forum acusticum 2026
8-12 September · Graz, Austria

EXPLORING INCOHERENT SCATTERING FROM A DYNAMIC WATER SURFACE

Sean G. Horsman[1], Eoin A. King[1,2]

[1] *The Galway Sound Lab, Department of Mechanical Engineering, University of Galway, Ireland*
[2] *The Ryan Institute, University of Galway, Ireland*

Abstract

Environmental sound propagation over water is usually modelled by treating the surface as acoustically hard and, perhaps more importantly, stationary. This simplification does not account for the possible influence of surface motion on the coherence of the surface-reflected sound field. In these tests, surface motion was generated using a simple ripple-making system in an outdoor shallow-water basin, allowing a range of ripple states to be produced. While maintaining a fixed acoustic source–receiver geometry, transfer-function (TF) measurements above the water surface were used to identify changes in the reflected sound field. For each measurement, water-surface activity was characterised by approximate ripple height and wavelength. The results showed that increasing water-surface activity deepened the incoherence around sensitive frequency bands associated with the source–receiver geometry.

Keywords: *reflection coherence, scattering, dynamic water surface, sea surface roughness, low-frequency*

1. Introduction

Offshore wind capacity and project development continue to expand globally [1] and so investigations into environmental noise propagation over the sea surface are becoming increasingly necessary. In propagation models, the water surface is traditionally treated as a hard reflecting ground [2], [3], [4]. This assumption is reasonable for calm seas when there is much more potential for specular reflection that will make a strong contribution to the propagated soundfield. In the literature, Bolin et al. note that calm sea surfaces are almost totally reflecting, [5] and Van Renterghem et al. describe these calm surface propagation conditions as a ”worst case scenario” in the case of offshore wind turbine (OWT) piling noise [6].

Obviously, the sea surface is rarely flat or stationary. Wind-driven waves and ripples change how the reflected field is projected on to a receiver. Bolin et al. also describe rough sea surfaces as producing non-specular, or incoherent scattering of the reflected sound [5]. In terms of ground attenuation, Boulanger and Attenborough, Van Renterghem et al. and Vecchiotti et al. have all described rough-sea effects through effective or equivalent impedance approaches where the roughness scales are small compared to the acoustic wavelengths [6], [7], [8].

In the past, periodically corrugated surfaces have been used as simplified models for examining how surface geometry redistributes a reflected acoustic field. Uretsky calculated reflection coefficients for a plane wave incident on a sinusoidal surface, providing comparison with experimental and approximate solutions [9]. Although this study considered a pressure-release boundary, the same sinusoidal geometry could provide a useful reference for airborne reflection from a sinusoidal high-impedance boundary. Fortuin's review identified sinusoidal-boundary methods as an important branch of sea-surface scattering theory and emphasised the combined roles of acoustic frequency, surface motion and source–receiver geometry [10]. Later, Chesneaux and Wirgin revisited the corrugated-surface problem for conditions in which the acoustic wavelength is comparable to the characteristic surface dimensions, including cases with substantial surface slope [11].

2. Aim of the Study

The aim of this small-scale study was to use a transfer-function (TF) method to explore measurable changes in the coherence of a surface-reflected sound field produced by different states of a dynamic water surface. Attention was given to the influence of ripple geometry, including surface height and water-surface wavelength. Within the available experimental conditions, for the lower part of our measurable acoustic spectrum, the

Corresponding author: *[s.horsman@universityofgalway.ie].*

water-surface wavelength, and acoustic wavelength, are of similar order . This places the experiment within the broader scope of corrugated-surface studies by Chesneaux and Wirgin, in which the incident wavelength is comparable to the characteristic surface dimensions, but with the additional complication of periodic surface motion.

3. Methodology

3.1. Basin Set Up, Acoustic Geometry and Water Surface Movement

The measurements were performed over an outdoor water basin using a fixed source–receiver arrangement as shown in Fig. 1. The horizontal distance between the source and microphone positions was 1.0 m with the source positioned 0.2 m above the mean water surface and the two vertically separated microphones at heights of 0.1 m and 0.2 m. This two-microphone arrangement was based on the geometry B described in ANSI S1.18:2018 [12], but with the lower mic raised slightly for practicality.The source and microphone positions remained fixed for all measurements. Each microphone was recorded to a channel of digital audio.

Two bespoke resistance-type probes were positioned at the edge of the basin with a horizontal separation of 0.465 m. The probes were connected to an NI USB-6211 data-acquisition interface and MATLAB to record the water-surface elevation. A simple motor-driven crank-and-connecting-rod paddle mechanism was installed at one end of the basin to generate ripples propagating in the same direction as the acoustic field. The paddle spanned the basin width to produce approximately plane progressive sinusoidal ripples along its length. The flat-water depth was 0.15 m. The basin was not filled entirely so that ripples could propagate without spilling over the side. A simple controller was used to produce a series of moving-surface conditions. A UT363 anemometer measured the wind speed and air temperature concurrently with the tests.

Initially, the TF was measured over the surface when there was no ripple activity. This result was labelled as "Flat-1" and formed the baseline measurement for later analysis. Subsequent TF measurements were then made over a range of different ripple states, each created by a new "level" on the paddle controller. There were no detents on the controller pot, and so each level was an arbitrary rotary change.

3.2. Dynamic Surface Description

Each measured voltage signal recorded via the two resistance probes positioned along the basin was converted to water-surface elevation using a probe calibration performed in the Hydrodynamics Laboratory at the University of Galway.

A fast Fourier transform (FFT) was applied to each calibrated probe signal. Frequency components below 1 Hz, including voltage drift and any zero-frequency component, were thus removed. The remaining filtered time-domain signal, $\eta_j(t)$, was then recovered by inverse FFT.

Figure 1: Water basin set up showing the source loudspeaker, microphones, ripple height probes and ripple generator.

3.2.1. Ripple height.

The RMS surface elevation was calculated separately for each probe as

$$\eta_{\mathrm{rms},j} = \sqrt{\frac{1}{N}\sum_{n=1}^{N} \eta_j^2[n]}, \tag{1}$$

where N is the number of samples. The ripple-height descriptor used in the analysis, η_{rms}, was the average of the two individual probe RMS values.

3.2.2. Ripple wavelength.

The power spectral density (PSD) of each calibrated ripple signal was calculated, and the three dominant ripple frequencies, f_w, were identified from peaks in the filtered spectra. For each dominant frequency, the finite-depth Airy wave equation

$$\omega_w^2 = g k_w \tanh(k_w h) \tag{2}$$

was solved numerically for k_w, where $\omega_w = 2\pi f_w$, g is acceleration due to gravity, and h is water depth. Following that, the ripple wavelength, Λ_w, was calculated as

$$\Lambda_w = \frac{2\pi}{k_w}. \tag{3}$$

3.3. Acoustic Measurements

The transfer function (TF) between the upper and lower microphones was measured using Smaart over the frequency range 250 Hz–9000 Hz. Measurements were first made for the flat-water reference condition, and then repeated for each dynamic surface condition using a 10 s averaging period.

The complex transfer function may be expressed as

$$H(f) = \frac{X_{\mathrm{u}}(f)}{X_{\mathrm{l}}(f)}, \tag{4}$$

where $X_{\mathrm{u}}(f)$ and $X_{\mathrm{l}}(f)$ are the complex spectra measured by the upper and lower microphones, respectively.

The magnitude-squared coherence between the microphone signals was calculated as

$$\gamma_{\mathrm{ul}}(f) = \frac{|G_{\mathrm{ul}}(f)|}{\sqrt{G_{\mathrm{uu}}(f)\, G_{\mathrm{ll}}(f)}}, \quad (5)$$

where $G_{\mathrm{ul}}(f)$ is the cross-power spectral density between the upper and lower microphone signals, and $G_{\mathrm{uu}}(f)$ and $G_{\mathrm{ll}}(f)$ are their respective auto-power spectral densities. The spectral estimates were temporally averaged over the 10 s measurement period.

4. Results and Analysis

The mean air temperature and wind speed during testing were 19.1 °C and 1.2 m s^{-1}, respectively.

4.1. Surface Characterisation

The measured surface conditions are summarised in Fig. 2. The ripple-generation system only produced a range of distinct surface states rather than precisely controlled ripple conditions. The case labels were assigned for identification only and do not represent a progressive increase in ripple height or overall surface activity. Comparisons between cases were therefore based on the measured RMS surface elevation and water-surface wavelength rather than on the numerical order of the case labels.

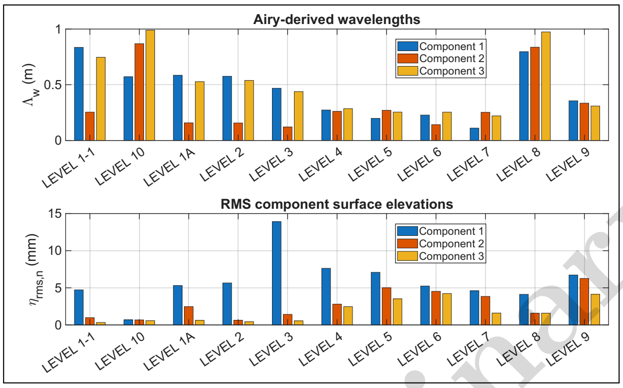

Figure 2: Airy-derived wavelengths and RMS heights of the three dominant ripple components identified for each measured surface condition.

The tests progressed in the numerical order shown in the plot, except for Level 10 which was a repeat "Flat" water condition performed at the end. Blue, red and orange bars (shown from left to right in each case) reveal approximate ripple wavelength and height components of the first three dominant ripples measured in the basin. A general pattern of decreasing ripple wavelength can be observed, which concurs with the increase in speed of the motor driving the ripple paddle. This happens until Level 8 when the paddle motor was slowed down for a measurement, then speeded up for another TF case at level 9. As stated previously, Level 10 was the last TF observation and a repeat of the flat water condition at the outset.

The ripple height pattern differs to that of the wavelength; in these cases there appears to be a strong monotonic component until level 3 after which the second and third components become relatively equivalent in magnitude to the first dominant component. In a visual observation of the basin at level 3 the water ripples appeared to be approaching a resonant frequency- the ripple height was discernibly the highest of all the cases- however the wave was not stationary.

4.2. Acoustic Results

The measured transfer-function results are shown in Fig. 3 and are smoothed for clarity. The test set up was such that unwanted reflections were present in the TF measurements caused by the exposed edge of the basin. To account for this, the FLAT-1 transfer function was used as the reference condition and all subsequent measurements were expressed relative to it. Changes observed in the relative transfer functions could therefore be attributed primarily to differences in the water-surface state for each test case. Changes to the flat-water reference were expressed generally as

$$\Delta Q(f) = Q_{\mathrm{Flat-1}}(f) - Q_{\mathrm{Case}}(f), \quad (6)$$

where Q represents TF magnitude, phase or coherence. Each of the TF change cases is shown in Fig. 4.

It can be seen that there are differences for each case. The largest changes occur predominantly between 3 kHz and 6 kHz, with the greatest overall difference observed for Level 3. The smallest difference occurs for Level 10 - the flat surface retest, while Levels 1-1 and 8 also show relatively small changes.

Levels 1A and 2 show modest differences, while Levels 4, 5, 6, 7 and 9 form a group with generally greater changes relative to the flat-water reference.

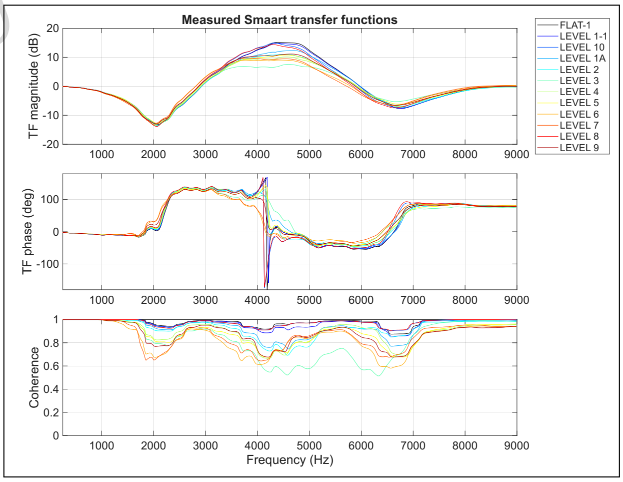

Figure 3: TF magnitude, phase and coherence for each of the surface ripple states.

4.3. Combined Analysis

To compare the acoustic response with the measured surface conditions, a simple surface-activity index was formed from the RMS surface elevation and mean water-surface wavelength:

$$I_{\mathrm{SA},j} = \frac{\eta_{\mathrm{rms},j}}{\bar{\Lambda}_{w,j}}, \quad (7)$$

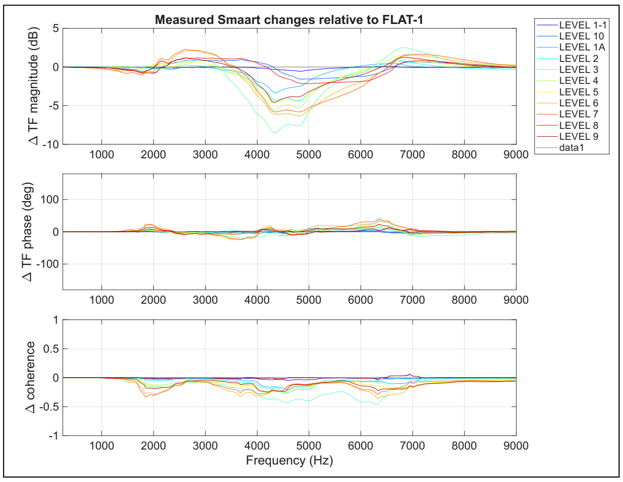

Figure 4: TF magnitude, phase and coherence relative to those of the FLAT-1 case.

where $I_{\mathrm{SA},j}$ is the surface-activity index for test case j, $\eta_{\mathrm{rms},j}$ is the RMS surface elevation, and $\overline{\Lambda}_{w,j}$ is the mean water-surface wavelength. The index increases for greater surface elevation or shorter surface wavelength and is used here only as a relative measure of activity.

The coherence difference relative to the flat-water reference condition was calculated at each frequency as

$$\Delta\gamma_j(f) = \gamma_{\mathrm{ref}}(f) - \gamma_j(f), \tag{8}$$

where $\gamma_j(f)$ is the coherence measured for test case j, and $\gamma_{\mathrm{ref}}(f)$ is the coherence measured for the FLAT-1 reference condition.

The overall coherence change was represented by the mean absolute difference across the full measured frequency range:

$$\overline{|\Delta\gamma_j|} = \frac{1}{N_f}\sum_{n=1}^{N_f} |\gamma_{\mathrm{ref}}(f_n) - \gamma_j(f_n)|\,, \tag{9}$$

where f_n is the frequency of the nth spectral bin, and N_f is the number of frequency bins included in the calculation.

The calculated values are summarised in Table 1 and Figs. 5 and 6. Figure 5 compares the surface-activity index and mean absolute coherence change for each case, while Fig. 6 shows the relationship between these quantities directly. Together, these results support the general pattern observed in the transfer-function data: greater surface activity tends to produce a larger coherence change, although the relationship is not strictly monotonic.

The linear fit gave $R^2 = 0.77$, indicating that the surface-activity index accounted for a substantial proportion of the variation in the mean absolute coherence change across the measured cases.

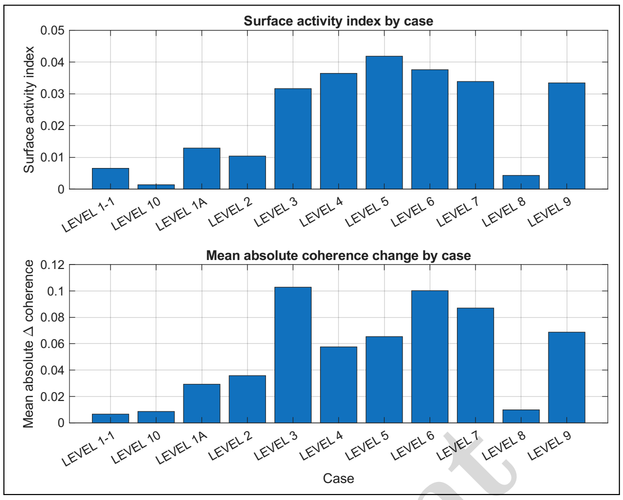

Figure 5: Surface-activity index and mean absolute coherence change for each test case.

Table 1: Surface-activity index and mean absolute coherence change for each test case.

Case	I_{SA}	$\overline{\lvert\Delta\gamma\rvert}$
LEVEL 5	0.0418	0.0654
LEVEL 6	0.0376	0.1002
LEVEL 4	0.0364	0.0576
LEVEL 7	0.0339	0.0870
LEVEL 9	0.0334	0.0687
LEVEL 3	0.0316	0.1028
LEVEL 1A	0.0129	0.0293
LEVEL 2	0.0104	0.0358
LEVEL 1-1	0.0066	0.0066
LEVEL 8	0.0043	0.0098
LEVEL 10	0.0014	0.0086

5. Discussion

The results show that movement of the water surface altered the coherence of the measured surface-reflected sound field. The smallest changes occurred for the repeat flat-water condition and the least active surface cases, while larger surface-activity indices generally corresponded to greater coherence change.

The relationship is not strictly monotonic, indicating that the simple surface-activity index does not describe every aspect of the acoustic response. As seen in Fig. 4, the coherence response contains three distinct regions of increased sensitivity, centred approximately at 2 kHz, 4.5 kHz and 6.5 kHz. These regions coincide with constructive and destructive interference features associated with the fixed source–receiver geometry. Increasing surface activity appears to affect the coherence most strongly within these regions, while the remainder of the spectrum is less strongly affected. This suggests that the influence of the moving surface is governed not only by the surface state, but also by the frequency-dependent sensitivity of the measurement geometry.

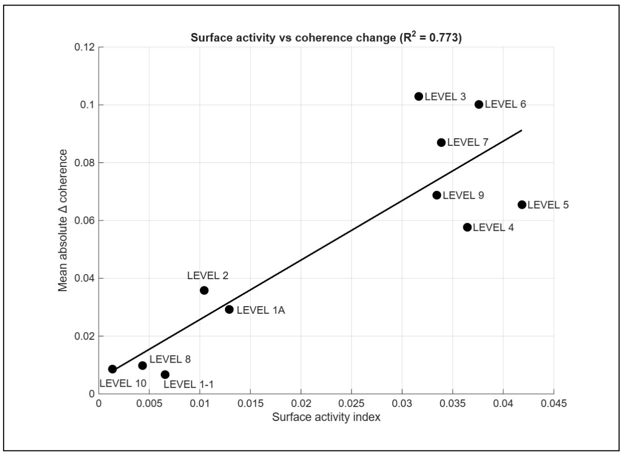

Figure 6: Mean absolute coherence change plotted against the surface-activity index. The solid line shows the linear least-squares fit, with the corresponding R^2 value shown on the figure.

As shown in Fig. 7, the coherence-sensitive response begins as the acoustic wavelength becomes shorter than the measured water-surface wavelength. This suggests that the ratio Λ_w/λ_a may mark a change in the interaction regime. However, the concentration of the response within distinct frequency regions indicates that the source–receiver geometry remains an important controlling factor.

The broadband coherence-change value should therefore be interpreted as a comparative indicator between cases rather than as a complete description of the frequency-dependent acoustic response.

The experiment was intentionally exploratory and used a single fixed source–receiver geometry within a small basin. The surface states were not precisely controlled, and the surface-activity index combines only RMS surface elevation and mean ripple wavelength. The results should therefore not yet be generalised to other geometries or full-scale sea conditions.

6. Conclusions

This exploratory study showed that motion of the water surface can alter the coherence of a surface-reflected sound field. Increasing surface activity generally produced greater coherence loss, concentrated within frequency-sensitive regions associated with the fixed source–receiver geometry. These regions occurred mainly where the acoustic wavelength was shorter than the measured water-surface wavelength, suggesting that both the surface scale and measurement geometry influence the response. The results indicate that treating the water surface as stationary may overlook important coherence effects.

Further work should independently vary ripple height and wavelength across a wider range of controlled surface states and source–receiver geometries, including shorter values of Λ_w, to determine whether the observed coherence-sensitive regions change due to a measurable effective surface impedance.

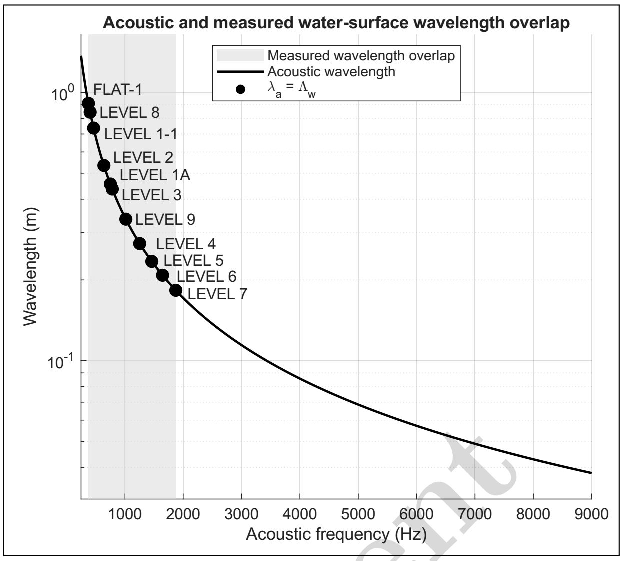

Figure 7: Comparison of acoustic wavelength with the mean measured water-surface wavelength for each moving-surface condition. The shaded region indicates the range over which the wavelengths overlap.

7. Acknowledgments

This research was funded by the Sustainable Energy Authority of Ireland (SEAI) under the ASHORE project as part of the National Energy Research Development and Demonstration (RD&D) Funding Programme 2022

References

[1] Global Wind Energy Council, "Global offshore wind report 2026," Global Wind Energy Council, Tech. Rep., 2026, Available at: `https://www.gwec.net/reports/globaloffshorewindreport`, accessed 3 July 2026.

[2] International Organization for Standardization, "Acoustics — attenuation of sound during propagation outdoors — part 2: General method of calculation," ISO, Geneva, Switzerland, Tech. Rep. ISO 9613-2:2024(E), 2024, Third edition. [Online]. Available: `https://www.iso.org/standard/86958.html`

[3] European Commission. Joint Research Centre. ICHP., *Common Noise Assessment Methods in Europe (CNOSSOS-EU): To Be Used by the EU Member States for Strategic Noise Mapping Following Adoption as Specified in the Environmental Noise Directive 2002/49/EC.* LU: Publications Office, 2012. Accessed: Sep. 22, 2023.

[4] B. Plovsing, "Nord2000. Comprehensive Outdoor Sound Propagation Model. Part 1: Propagation in an Atmosphere without Significant Refraction," DELTA Acoustics & Vibration, Hørsholm, Denmark, Tech. Rep. AV 1849/00, 2006, Revised report.

[5] K. Bolin, M. Boué, and I. Karasalo, "Long range sound propagation over a sea surface," *The Journal of the Acoustical Society of America*, vol. 126, no. 5, pp. 2191–2197, 2009. DOI: 10.1121/1.3238236

[6] T. Van Renterghem, D. Botteldooren, and L. Dekoninck, "Airborne sound propagation over sea during offshore wind farm piling," *The Journal of the Acoustical Society of America*, vol. 135, no. 2, pp. 599–609, 2014. DOI: 10.1121/1.4861244

[7] P. Boulanger and K. Attenborough, "Effective impedance spectra for predicting rough sea effects on atmospheric impulsive sounds," *The Journal of the Acoustical Society of America*, vol. 117, no. 2, pp. 751–762, 2005. DOI: 10.1121/1.1847872

[8] A. Vecchiotti, T. J. Ryan, J. F. Vignola, and D. Turo, "Atmospheric sound propagation over rough sea: Numerical evaluation of equivalent acoustic impedance of varying sea states," *Acoustics*, vol. 6, no. 2, pp. 489–508, 2024. DOI: 10.3390/acoustics6020026

[9] J. L. Uretsky, "Reflection of a plane sound wave from a sinusodial surface," *The Journal of the Acoustical Society of America*, vol. 35, no. 8, pp. 1293–1294, 1963. DOI: 10.1121/1.1918690

[10] L. Fortuin, "Survey of literature on reflection and scattering of sound waves at the sea surface," *The Journal of the Acoustical Society of America*, vol. 47, no. 5B, pp. 1209–1228, 1970. DOI: 10.1121/1.1912022

[11] J.-M. Chesneaux and A. Wirgin, "Reflection from a corrugated surface revisited," *The Journal of the Acoustical Society of America*, vol. 96, no. 2, pp. 1116–1129, 1994. DOI: 10.1121/1.410386

[12] Acoustical Society of America, "ANSI/ASA S1.18-2018: Method for Determining Acoustic Impedance and Absorption of Ground Surfaces Using a Two-Microphone Method," Acoustical Society of America, New York, USA, Tech. Rep., 2018. [Online]. Available: https://standardsstore.acousticalsociety.org/standards/ansi-asa-s1-18-2018/